THE JOURNAL OF PHYSICAL CHEMISTRY C

Article

Cite This: J. Phys. Chem. C 2019, 123, 16883−16892

pubs.acs.org/JPCC

Surface Reconstruction under the Exposure of Electric Fields Enhances the Reactivity of Donor-Doped $SrTiO_3$

Buğra Kayaalp,[†] Kurt Klauke,[†] Mattia Biesuz,[‡] Alessandro Iannaci,[§] Vincenzo M. Sglavo,[‡] Massimiliano D'Arienzo,[∥] Heshmat Noei,[⊥] Siwon Lee,[#] WooChul Jung,[#] and Simone Mascotto*[,†]

[†]Institut für Anorganische und Angewandte Chemie, Universität Hamburg, Martin-Luther-King-Platz 6, 20146 Hamburg, Germany

[‡]Dipartimento di Ingegneria Industriale, Università degli Studi di Trento, Via Sommarive 9, 38123 Trento, Italy

[§]INSTM, Trento Research Unit, Via G. Giusti 9, 501211 Florence, Italy

[∥]Dipartimento di Scienze dei Materiali, Università di Milano-Bicocca, Via R. Cozzi, 55, 20125 Milano, Italy

[⊥]Deutsches Elektronen-Synchrotron DESY, Notkestr. 85, 22607 Hamburg, Germany

[#]Department of Materials Science and Engineering, Korea Advanced Institute of Science and Technology, 291 Daehak-ro, Yuseong-gu, Daejeon 34141, Republic of Korea

Supporting Information

ABSTRACT: In the present work, we show how exposure to electric fields during a high-temperature treatment can be used to manipulate surface properties of donor-doped ceramics and thus improve their reactivity. $La_{0.1}Sr_{0.9}TiO_3$ (LSTO) nanoparticles, prepared by hydrothermal synthesis, were consolidated under air with and without external electric fields. Although neither approaches caused grain growth upon consolidation, the treatment under the influence of the electric field (i.e., flash sintering) remarkably enhanced the segregation of Sr on the material's surface. In addition, a high concentration of O^- defects both in bulk as well as on the material surface was demonstrated by spectroscopic methods. This enhanced defect concentration along with the nanoscopic grain size of the field-consolidated materials is probably one of the triggering factors of their improved charge carrier mobility, as observed by impedance spectroscopy. The effect of such a perturbed defect structure on the reactivity of the materials was evaluated by the total oxidation of methane. For materials treated under the influence of electric fields, the catalytic reaction rate improved by a factor of 3 with respect to that of conventionally treated LSTO, along with a remarkable decrease of the activation energy. Thus, electric-field-assisted processes, usually known for their energy-saving character, can also be deemed as an attractive, forward-looking strategy for improving functional properties of ceramics.

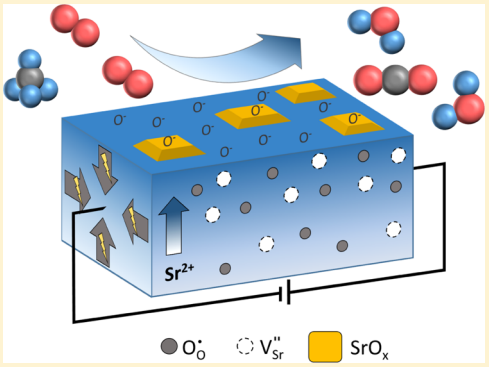

INTRODUCTION

The employment of field-assisted methods for preparation and processing of functional materials attracted considerable attention in past years. The faster heat development and propagation enables significantly reduction of the reaction time and furnace temperature, thus providing more sustainable and greener solutions with respect to conventional approaches.[1] Along with microwave syntheses, which continue to play a central role since the last 10 years,[2−4] the employment of electric and magnetic fields emerged as an alternative for the preparation and manufacture of inorganic materials.[5] Aside from the environmentally friendly character, the exposure of matter to such fields has shown to be a powerful tool to design materials with specific microstructures[6−8] and to control defect formation[9,10] and mobility,[11] thus motivating a fast growing interest around these approaches.[5,12−14]

For many high-temperature applications, such as solid oxide fuel cells, thermoelectrics, or catalysis, the consolidation of the ceramic materials is an important technological requirement. In this respect, the application of high voltage and current to a ceramic green body during heating-induced stabilization and consolidation at much lower furnace temperatures than those used in conventional treatments and only within few seconds/minutes has been shown.[15] Local overheating of the material via the Joule effect has been proposed as one of the reasons for such rapid process, also known as flash sintering.[16,17] Obviously, the electrical properties of the ceramics play a central role in the treatment conditions. Dielectric materials such as $SrTiO_3$ consolidate at temperatures around 1000 °C,[18] whereas conductive systems like iron- or cobalt-based oxides, near room temperature.[19] One well-known strategy to vary the electrical response of ceramics accurately is given by doping with aliovalent ions. As reported by Shomrat et al.,[20] a clear dependency exists between the doping grade of the p-type

Received: May 15, 2019
Revised: June 13, 2019
Published: June 13, 2019

DOI: 10.1021/acs.jpcc.9b04620
J. Phys. Chem. C 2019, 123, 16883−16892

conductor $SrTi_{1-x}Fe_xO_3$ ($0 \leq x \leq 0.03$) and the onset temperature of consolidation at different applied voltages, showing that the consolidation mechanism is dependent on the sample resistance.

Additionally, the exposure to direct current (DC) electric fields can have also a remarkable effect on the point defect properties of ceramics, especially if doped. As found by Escrig et al.,[21] in $SrTi_{1-x}Mg_xO_3$ ($0 \leq x \leq 0.01$), when small electric fields are applied, the underbonded oxide ions adjacent to substitutional Mg^{2+} ions ionize readily to O^-, generating a conductive state dominated by p-type conduction. In another work, similar hole conductivity and ionization of underbonded O^{2-} were obtained for $BaTi_{1-x}Ca_xO_3$ under exposure of a dc bias.[22] Interestingly, these effects were negligible for $SrTiO_3$ and $Ba_{1-x}Ca_xTiO_3$, pointing out the high significance of the aliovalent substitution.

Besides inducing remarkable variation of the conductive properties, the perturbation of the defect structure of ceramics when electric fields are applied has profound effects on their chemical reactivity. A few decades ago, the so-called nonfaradaic electrochemical modification of the catalytic activity (NEMCA) approach emerged as a strategy for the controlled promotion of an oxide-supported catalyst under the influence of an external voltage.[23] In the NEMCA process, oxygen anions are electrochemically pumped from the counter electrode to the polarizable oxide−catalyst interface, where they accumulate and dissociate to O^-. These paramagnetic defects diffuse all over the catalyst surface, increasing the catalyst work function, thus resulting in dramatic changes in catalytic activity and selectivity.[24]

In the last years, several reports pointed out how specific modification of the surface morphology and surface chemistry of $SrTiO_3$ engendered strong alteration of its catalytic properties.[25−28] Very recently, we showed that the consolidation of $SrTiO_3$ nanoparticles under the assistance of strong electric fields improved their surface reactivity, enabling higher catalytic conversion of methane.[29] Such enhanced properties were ascribed to the larger extent of Sr segregation induced by the field-assisted treatment, which led to a defect structure perturbation of the materials surface. In other works, it has been reported that Sr enrichment in surface-reconstructed $SrTiO_3$ had beneficial effects toward methane oxidation.[25,30,31]

In this contribution, we show how surface reactivity and defect properties are enhanced when $SrTiO_3$ doped with donor species such as La^{3+} undergoes an electric field-assisted treatment. La-doped $SrTiO_3$ (LSTO) was chosen because of its importance for applications in energy conversion.[32,33] The materials were prepared in the form of nanoparticles with the stoichiometry of $La_{0.1}Sr_{0.9}TiO_3$ (LSTO) by means of a hydrothermal method, thus providing high chemical purity and controlled particle morphology.[34,35] For evaluation of the material reactivity, total methane oxidation was employed as a typical high-temperature model test reaction.

The surface reactivity of perovskite oxides can be easily modified during high-temperature treatments because of cationic segregation phenomena.[36] Herein, we show that the combination of high temperature and electric field exposure determines massive segregation of Sr on the LSTO surface along with enhanced concentration of O^- ions. Such a perturbation of the defect structure strongly modified the reactivity and conductivity mechanism of the materials, thus resulting in a remarkable improvement of the catalytic performance. Hence, besides the energy-saving character, the consolidation of ceramics under the assistance of an electric field can be considered as a valuable tool to tune their defect properties and improve their functional character.

EXPERIMENTAL PART

Materials. Strontium acetate hemihydrate (98%, $Sr(OOCCH_3)_2{\cdot}0.5H_2O$), titanium (IV) isopropoxide (97+%, $Ti[OCH(CH_3)_2]_4$), and lanthanum (III) nitrate hexahydrate (99.9%, $La(NO_3)_3{\cdot}6H_2O$) were purchased from Alfa Aesar. Ethanol (99.9%, C_2H_6O) was purchased from VWR Chemicals. Glacial acetic acid ($C_2H_6O_2$) was purchased from Fisher Chemicals. Sodium hydroxide (98.5%, NaOH) was purchased from Acros Organics. All chemicals were used as received without further purification.

Synthesis of $La_{0.1}Sr_{0.9}TiO_3$ Nanoparticles. $La_{0.1}Sr_{0.9}TiO_3$ (LSTO) nanocuboids were prepared by modification of the hydrothermal synthesis route described in the work of Ouyang et al.[37] In a typical synthesis, stoichiometric amounts of lanthanum nitrate hexahydrate ($La(NO_3)_3{\cdot}6H_2O$) and titanium (IV) isopropoxide ($Ti[OCH(CH_3)_2]_4$) were dissolved in ethanol. A second solution with a stoichiometric amount of strontium acetate hemihydrate ($Sr(OOCCH_3)_2{\cdot}0.5H_2O$) in glacial acetic acid was added slowly to the first solution. The resulting sol was stirred for 1 h at room temperature. Subsequently, the solvents were evaporated under continuous stirring at 75 °C. The obtained gelatin was ground to white powder. An appropriate amount of powder was added to a 10 mL Teflon liner, and a 1 M NaOH solution was added up to 80% of the liner's total volume. The Teflon-lined stainless steel autoclave was placed in an oven under autogeneous pressure for 24 h at 170 °C and then allowed to cool down. The precipitate was washed thoroughly with deionized water and dried at 80 °C overnight.

Consolidation Treatments. Cylindrical pellets (diameter = 8 mm, thickness ∼3 mm) were shaped by uniaxial pressing at 350 MPa. The two flat surfaces of the green components were painted using carbon-based conductive cement (Plano GmbH) and then subjected to electric field exposure. The process was carried out in a modified dilatometer (Linseis L75) at a heating rate of 20 °C min^{-1}. The samples were placed between two platinum disks (diameter = 9 mm, thickness ∼3 mm), which were connected to a DC power supply (Glassman EW 5 kV, 120 mA) and to a multimeter (Keithley 2100). The electrical parameters (current and voltage), the furnace temperature, and the displacement of the dilatometric piston were recorded at 1 Hz. The consolidation experiments were carried out using electric fields of 300 and 600 V cm^{-1} and a current limit of 2.5 mA mm^{-2}; once the current limit was reached upon the so-called flash event, the current was let to flow through the ceramic components for 30 s and then the power supply and the dilatometer furnace were switched off. Note that a low current limit was chosen in this work to limit the consolidation to the early sintering stages. Conventionally consolidated bodies were manufactured with the following firing program: from room temperature to 900 °C with a 5 °C min^{-1} ramp, from 900 to 1150 °C with a 0.5 °C min^{-1} ramp, and holding at 1150 °C for 4 h and free cooling in the furnace.

The bulk densities of the samples were measured as the ratio between the weight and the volume (determined by a digital caliper). The relative density (ρ) was calculated in % using a value of 5.26 g cm^{-3} for fully dense $La_{0.1}Sr_{0.9}TiO_3$.

Samples were labeled as follows: as-prepared (AP) $La_{0.1}Sr_{0.9}TiO_3$; conventionally treated (CS) $La_{0.1}Sr_{0.9}TiO_3$; and

DOI: 10.1021/acs.jpcc.9b04620
J. Phys. Chem. C 2019, 123, 16883−16892

$La_{0.1}Sr_{0.9}TiO_3$ treated with the assistance of an electric field (FS − x), where x = 300 or 600, depending on the magnitude of the field.

X-ray Diffraction. X-ray diffraction analysis was carried out with an X'Pert Pro diffractometer (PANalytical Corp.) with 1.5406 Å Ni-filtered Cu Kα radiation, operating at 45 kV and 40 mA, step size of 0.0130°, and step time of 74 s/step. The mean crystallite size was calculated from the full width at half-maximum of the most intense reflection using the Scherrer equation.

Gas Physisorption. Nitrogen physisorption isotherms were obtained at 77.4 K using a Quadrasorb SI-MP by Quantachrome. Outgassing was performed with a Masterprep Degasser (Quantachrome Corp.) at 120 °C for 12 h. Specific surface areas (SSAs) were determined with the Brunauer−Emmett−Teller method[38] at relative pressures p/p_0 = 0.07−0.3.

Electron Microscopy. Scanning electron microscopy (SEM) images were obtained on LEO1550 with a spatial resolution of ≈1 nm. The powder was fixed on a standard carbon conductive tab and was investigated without further conductive coating.

Transmission electron microscopy (TEM) measurements were carried out on JEOL JEM 2200 FS at 200 kV equipped with two CEOS Cs correctors (CETCOR, CESCOR), a Gatan 4K UltraScan 1000 camera, a high-angle annular dark field detector, and a JEOL JED-2300 Si(Li) energy dispersive X-ray (EDX) spectroscopy detector. The samples were crushed into fine powder, suspended in toluene by sonication, and dropped on a carbon-coated 400 mesh TEM grid. The excess solvent was removed with a filter paper and by drying the grid under air.

Energy dispersive X-ray (EDX) spectra were acquired from several analysis points on the particle, and average atomic ratios were calculated for each cation in the perovskite oxides. Analyses were repeated at least on three positions for each sample, and less than 1.0 atom % disparity was observed for surveyed cations at each point.

X-ray Photoelectron Spectroscopy (XPS). XPS measurements were carried out using a high-resolution two-dimensional delay line detector. A monochromatic Al Kα X-ray source (photon energy 1486.6 eV; anode operating at 15 kV) was used as incident radiation. XPS spectra were recorded in fixed transmission mode. Pass energy of 20 eV was chosen, resulting in an overall energy resolution better than 0.4 eV. Charging effects were compensated by using a flood gun. The base pressure in the measurement chamber was maintained at about 5×10^{-10} mbar. The binding energy scales were recalibrated based on the C 1s line from adventitious hydrocarbons at 284.8 eV.[39] Casa XPS software with a 70:30 Gaussian Lorentzian product function and Shirley background subtraction was used for peak deconvolution.

Electron Spin Resonance (ESR) Spectroscopy. The electron spin resonance (ESR) investigations were performed by using a Bruker EMX spectrometer operating at the X-band frequency and equipped with an Oxford cryostat working in the temperature range of 4−298 K. The samples were inserted in quartz glass tubes connected to a high-vacuum pumping system. Spectra were recorded under in vacuo conditions ($p < 10^{-5}$ mbar) at 130 K. The g values were calculated by standardization with α,α'-diphenyl-β-picryl hydrazyl. Care was taken to always keep the most sensitive part of the ESR cavity (1 cm length) filled. Spectra simulations and fits were performed using the SIM 32 program.[40]

Electrochemical Impedance Spectroscopy. Impedance measurements were performed using a Novocontrol alpha-A impedance analyzer connected to a NorECs Probostat sample chamber. A Novocontrol-HT controller connected to an type S thermocouple mounted next to the sample was employed for temperature control. A colloidal silver paste (Pelco) was applied on both sides of the analyzed pellets to ensure contact to the Pt net electrodes. Frequencies in the range of 10^{-2}−10^{7} Hz were employed with an amplitude of 100 mV_{rms} for all measurements. Novocontrol WinFIT was used for data evaluation and equivalent circuit fitting. An equivalent circuit consisting of three RQ elements usually ascribed to grain boundary, bulk, and electrode interface contributions was employed to fit the experimental data. The oxygen partial pressure was set by mixing Ar 5.0 with air using MKS MF-1 mass flow controllers. Partial pressures were monitored using a NorECs miniature oxygen sensor electrode with a sealed internal metal/metal oxide reference and a Rigol DM-3058 multimeter.

A constant gas flow of 19 sccm was employed for all measurements with the gas supply tube ending in close proximity to the sample. All samples were equilibrated for 13 h at the desired partial pressure. Each temperature was held for 3 h before a measurement was performed. Temperature was varied between 700−400 °C, whereas pO_2 was varied between 0.21−10^{-4} bar by adjusting the air/Ar atmosphere.

Temperature-Programmed Oxygen Desorption. Temperature-programmed desorption of oxygen (O_2-TPD) profiles was retrieved by a Micromeritics AutoChem 2920 analyzer. Before TPD, each sample (∼250 mg) was pretreated under 5% O_2 balanced in He (50 mL min^{-1}) at 550 °C for 2 h. After cooling to 50 °C, the TPD operation was carried out under a He carrier gas (30 mL min^{-1}) atmosphere from 50 to 900 °C at a heating rate of 10 °C min^{-1}. The amount of oxygen desorbed was monitored by a thermal conductivity detector.

Catalytic Oxidation of Methane. The catalytic measurements for CH_4 oxidation were carried out at atmospheric pressure with a fixed-bed flow quartz reactor with an internal diameter of 4 mm. In the catalytic bed, 100 mg of catalyst mixed with 200 mg of quartz sand was placed in between 100 mg of a quartz sand layer and a quartz wool layer was in the bottom supporting the system. The reaction temperature was monitored using a K-type thermocouple that was in contact with the catalytic bed. For methane oxidation, the reactant gas mixture consisting of 2 vol % CH_4, 4 vol % O_2, and 94 vol % Ar was used and fed at 50 mL min^{-1} corresponding to weight hourly space velocity of 30 000 mL g^{-1} h^{-1}. The light-off curves were measured during ramping temperature at 3 °C min^{-1}, after activation of the catalysts at 800 °C under the reaction atmosphere. The CH_4 conversion ratio (%) was calculated as 100 × (mol $CH_{4,in}$ − mol $CH_{4,out}$)/mol $CH_{4,in}$. The apparent activation energy (E_a) value was estimated from Arrhenius-type plots ($1000/T$ vs the reaction rate) and obtained below 10% conversion of methane. The reactant and product gases were monitored using a quadrupole mass spectrometer (Pfeiffer Vacuum GSD320) in real time. The conversion ratio of CH_4 was detected by the m/z = 15 peak instead of the 16 peak (the major peak of methane) to avoid the interference caused by the fragmented carbon monoxide (0.9%), water (1.1%), carbon dioxide (8.5%), and oxygen (11%). The mass concentration determination mode was used for all tests.

DOI: 10.1021/acs.jpcc.9b04620
J. Phys. Chem. C 2019, 123, 16883−16892

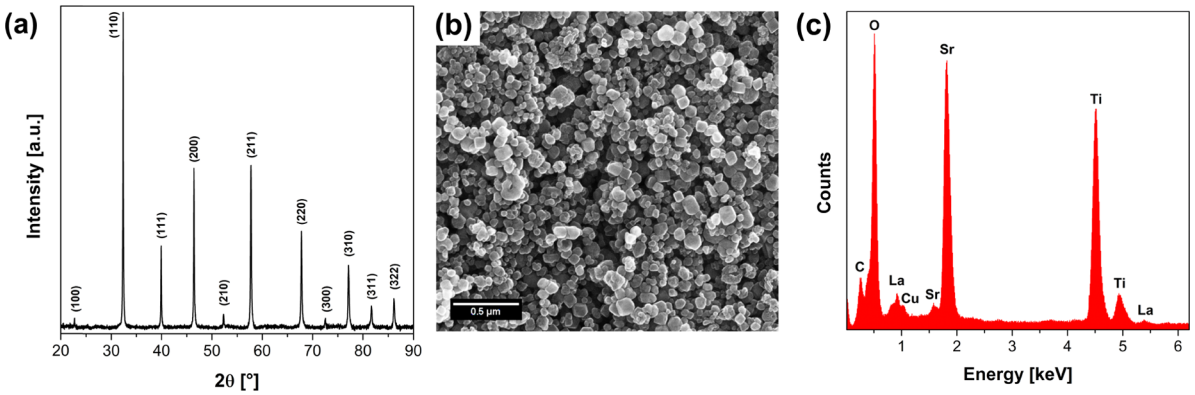

Figure 1. (a) X-ray diffractogram of as-prepared $La_{0.1}Sr_{0.9}TiO_3$ nanoparticles with the corresponding (b) SEM and (c) EDX analysis. Cu signals are originated by the TEM grid and do not belong to the sample composition.

Table 1. Physical and Catalytic Parameters for Investigated $La_{0.1}Sr_{0.9}TiO_3$ (LSTO) Systems: Average Crystallite Size (Φ) Calculated from XRD, Specific Surface Areas (SSAs) from Nitrogen Physisorption, Atomic Composition of the Investigated LSTO Systems Normalized to $La_{0.1}Sr_{0.9}TiO_3$ Nominal Stoichiometry, Ratio between the A and B Cations from EDX, Activation Energies for the Migration of Charge Carriers (E_a^{EIS}) Retrieved from Electrochemical Impedance Spectroscopy under Air, and Surface Area-Normalized Activation Energy (E_a^{Cat}) Values Retrieved from Methane Oxidation

	Φ [nm]	SSA [$m^2\ g^{-1}$]	La	Sr	Ti	(Sr + La)/Ti	E_a^{EIS} [eV]	E_a^{Cat} [kJ mol^{-1}]
AP	39	24	0.1	0.93	0.97	1.062		
CS	57	5	0.12	0.94	0.94	1.128	1.079 ± 0.007	124.1 ± 2.8
FS-300	56	9	0.11	1.03	0.86	1.33	0.942 ± 0.008	101.3 ± 3.4
FS-600	53	9	0.12	1.04	0.84	1.38	0.971 ± 0.004	103.9 ± 2.4

RESULTS AND DISCUSSION

La-doped $SrTiO_3$ nanoparticles were prepared by low-temperature hydrothermal synthesis and consolidated under air both using conventional and field-assisted approaches. The X-ray diffraction (XRD) results in Figure 1 show that as-prepared (AP) nanoparticles present phase pure cubic perovskite structure with an average crystallite size of 40 nm (Table 1). Electron microscopy analyses pointed out crystalline nanocuboids of size ranging between 50 and 100 nm (Figure 1). From the EDX elemental analysis (Figure 1c), the ratio between cations was determined, confirming the nominal La doping of 10% (Table 1). Substitution of La into the Sr lattice positions could be verified by the shift of the (110) reflection to higher angles with respect to pure $SrTiO_3$ (Figure S1).

Conventional treatment in a dilatometer oven was performed at 1150 °C over 4 h. During field-assisted treatments, the exposure to electric fields remarkably accelerated the oxide consolidation. Fields of 300 and 600 V cm^{-1} triggered in the materials the so-called flash event, i.e., sudden and vigorous consolidation within seconds, at 1190 and 980 °C, respectively (Figure S2). The specific surface area decreased from 24 $m^2\ g^{-1}$ for the as-prepared nanoparticles to 9 $m^2\ g^{-1}$ for the FS samples and 5 $m^2\ g^{-1}$ for the CS material (Table 1, Figure S3). Most likely, this difference is due to the much faster process of consolidation under field exposure, which does not give the system enough time to relax.

XRD analysis shows that in all high-temperature-treated samples the perovskite phase was retained (Figure 2a). The minor impurity phase observed for the FS-600 sample (e.g., 2θ = 38, 44, 64°) was successfully ascribed to metallic Ag (Figure S4), which stemmed from the contamination by colloidal silver paste used in the impedance spectroscopy analysis (see below) to ensure contact with Pt electrodes. The average crystallite size is substantially the same among all systems along with very modest growth in comparison with the as-prepared nanoparticles (Table 1). Such a grain growth arrest is usually observed for La-doped $SrTiO_3$ and is likely ascribed to the enhanced concentration of Sr vacancies caused by the substitution of La into the Sr site.[11,32]

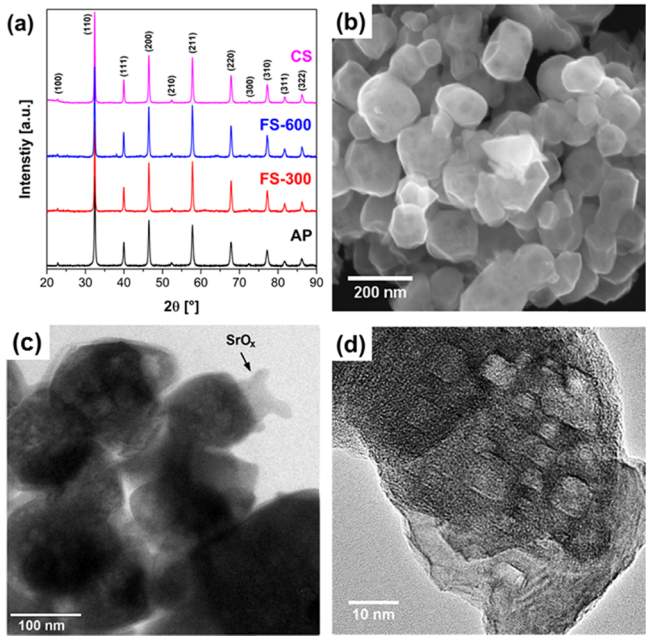

Figure 2. (a) X-ray diffraction patterns of investigated LSTO systems. SEM and TEM micgrographs of (b–c) FS-600 and (d) CS LSTO systems. Electron microscopy shows initial formation of higher contrast SrO-rich sites on perovskite surface for conventionally sintered LSTO (CS), whereas the SrO layer is significantly more pronounced for the flash-sintered material (FS-600).

DOI: 10.1021/acs.jpcc.9b04620
J. Phys. Chem. C 2019, 123, 16883−16892

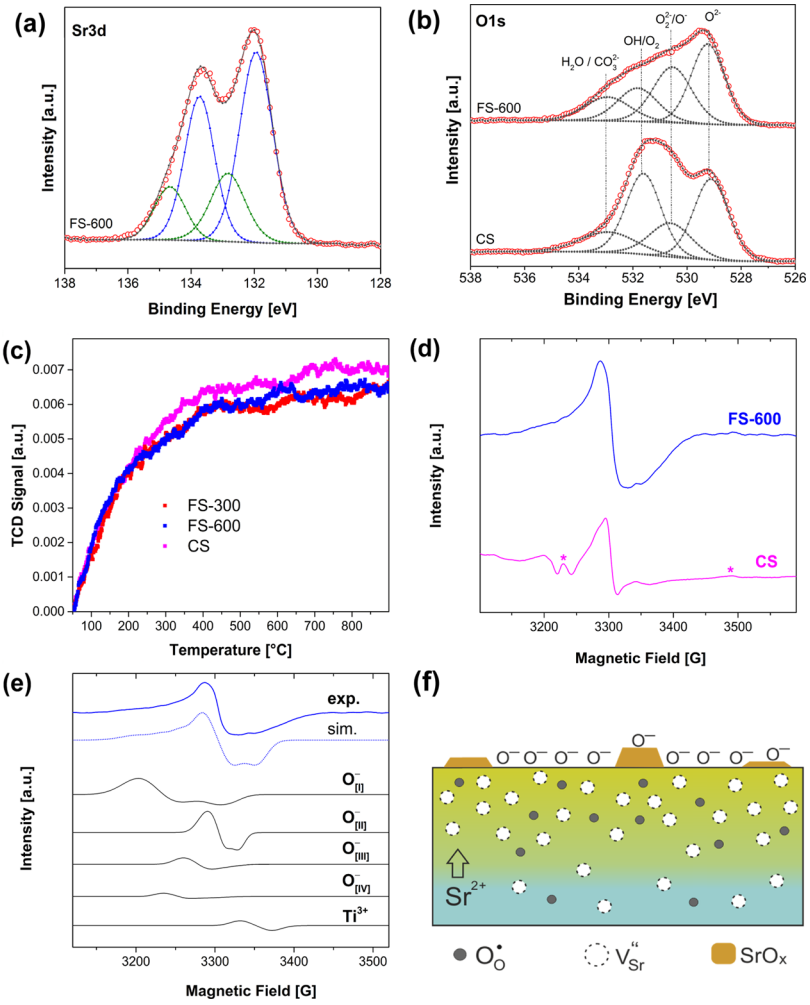

Figure 3. Spectroscopic analyses for differently processed LSTO samples: (a) Sr 3d region and (b) O 1s region of XPS spectra; (c) oxygen temperature-programmed desorption (TPD-O_2) profiles of differently processed LSTO samples; (d) ESR spectra at 130 K in vacuum with the asterisks denoting the Mn^{2+} defects; (e) magnification and simulation of the resonance occurring in FS-600 $La_{0.1}Sr_{0.9}TiO_3$: experimental (exp.) and simulated (sim.) spectra deconvolution of ESR signal into different paramagnetic species; (f) scheme for spatial distribution of different defect centers on electric field-treated LSTO particles.

Electron microscopy was employed to study the materials morphology (Figure 2b–d). Edged, angular particle aggregates of a similar shape result for all investigated materials in the powder state (Figures 2b and S5). The consolidation under exposure to electric fields also induced the formation of voluminous excrescences at the grain surface (Figure 2c). These were associated to a local SrO_x phase, as detected by TEM/EDX spectroscopy (Figure S6). Even if the assessment of the microstructure nature of this Sr-rich phase is not an easy task, the absence of any reflection in the XRD pattern, its undefined morphology, and low contrast, likely indicate its amorphous character.

By means of this method, the Sr segregation on the material surface depending on the type of high-temperature treatment was also investigated (Table 1). EDX has a high penetration depth and therefore is poorly suitable for accurate surface analysis. Nonetheless, the results clearly demonstrate the concentration increase of Sr, highlighting the large extent of the cationic segregation through the grain. These findings are also corroborated by XPS analyses (Figures 3a and S7), which confirmed the remarkable A-site segregation (cation ratio (Sr + La)/Ti = 2.4) and pointed out significant concentration of nonlattice Sr in the material treated under the influence of the electric field, ascribed to the formation, among others, of carbonate compounds.

The generation of SrO_x and other nonlattice Sr-based species, such as $SrCO_3$ and $Sr(OH)_2$, at the surface of Sr-based perovskites upon high-temperature treatments is largely confirmed in the literature.[41−45] Among the many reasons one possible explanation of the surface Sr enrichment can be given looking at the defect chemistry of $SrTiO_3$ expressed with the Kröger−Vink notation[46]

$$Sr_{sr} + O_o \rightarrow V''_{Sr} + V_O^{2\bullet} + SrO \quad (1)$$

In principal, a high-temperature treatment promotes the diffusion of strontium and oxygen from their lattice positions (Sr_{Sr}, O_o, respectively) to form strontium (V''_{Sr}) and oxygen vacancies ($V_O^{2\bullet}$). From the conservation of mass law, the formation of a SrO-rich phase (indicated here as one of the possible compositions) occurs and segregates at the grain surface and interface.[41,47] The generation of Frenkel defects, although theoretically possible, is considered here unfavored, due to the high energy demand for the highly packed perovskite lattice.[48,49] In La-doped $SrTiO_3$, an additional formation

DOI: 10.1021/acs.jpcc.9b04620
J. Phys. Chem. C 2019, 123, 16883−16892

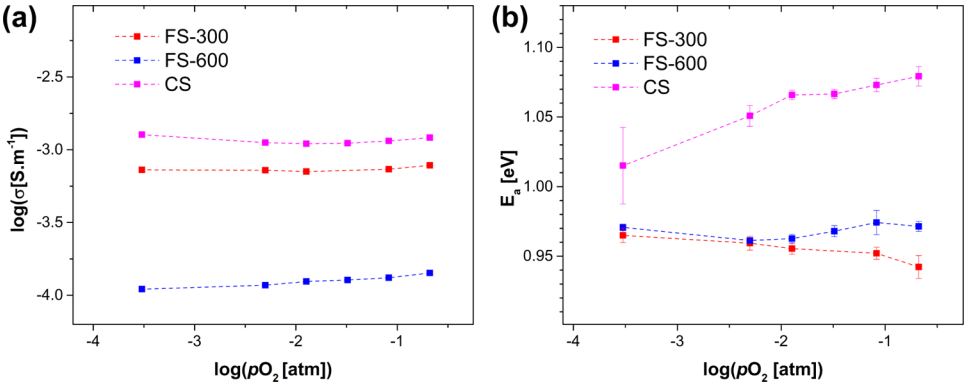

Figure 4. (a) Specific conductivity of the consolidate materials as a function of oxygen partial pressure at 700 °C and (b) calculated activation energies of charge carrier species determined from the conductivity Arrhenius-type plots.

mechanism of SrO was proposed.[43] The allocation of La^{3+} doping ions on the Sr^{2+} sites is compensated by the formation of electrons. During treatment under air, oxygen from the atmosphere gets reduced by the free electrons and reacts with the Sr ions of the top surface layer, originating a SrO phase.

In the case of the electric field-treated materials, the origin of the larger extent of Sr enrichment at the surface is not completely understood yet. It might be engendered by the localized thermal gradient at the microstructural level. As shown elsewhere, during electric field-assisted consolidation of insulating materials, local overheating[12] or even melting[50] of the grain boundaries occurs. Thus, such a temperature gradient in the grain might determine defect redistribution and impart the larger Sr segregation. However, an interplay between the electric field/current and the defect chemistry cannot be excluded. Field-induced defect perturbation has been often proposed as the main mechanism for field-assisted sintering of ceramics.[12,51,52]

If a surface Sr segregation occurs, Sr vacancies are evidently left behind. As the materials are consolidated under air, the concentration of these defects results to be much higher than that of O vacancies.[53,54] In this regard, temperature-programmed oxygen desorption (TPD) analyses showed that all LSTO materials present comparable desorption kinetics (Figure 3c). Very low release of oxygen was observed, especially for the ceramics exposed to the electric field, indicating low concentration of oxygen vacancies.

XPS was additionally adopted to gain insights into the surface chemistry of the oxygen species. In Figure 3b, the O 1s spectra of the materials treated conventionally and under the exposure of an electric field are shown. Besides the lattice oxygen component at ~529.1 eV, different surface oxygen contributions are found. These comprise highly oxidative oxygen species (O_2^{2-}/O^- at ~530.6 eV), hydroxyl groups or adsorbed oxygen (−OH or O_2 at ~531.6 eV), and physisorbed water or carbonates (H_2O or CO_3^{2-} at ~533 eV). Interestingly, it is noted that the influence of the electric field during consolidation enhanced the contribution of O_2^{2-}/O^- and decreased that of hydroxyl groups.

Considering the paramagnetic character of the O^- centers, further investigations were performed by means of ESR spectroscopy. Both materials treated conventionally and under field exposure show a complex spectrum, constituted by a broad anisotropic signal, which appears much more intense in the FS-600 sample (Figure 3d). This resonance is attributable to different superimposed oxygen species (M^{n+}/O^- species, where M = Sr^{2+}, Ti^{4+}) and Ti^{3+} centers. For FS-600, the signal was resolved into five different components (Figure 3e), whose g values and relative contributions were calculated by simulation (Table S1). Concerning the O^- centers with axial symmetry, the decrease of the $g_\perp$ value is related to the increasing strength of the metal−oxygen interaction.[55] Thus, the component of the signal with $g_\perp$ = 2.055 ($O_{[I]}^-$) is assigned to O^- adsorbed on SrO[56,57] whereas the other features ($O_{[II]}^-$, $O_{[III]}^-$, and $O_{[IV]}^-$) are attributable to holes trapped on oxygen adsorbed on Ti^{4+} centers most likely having different chemical environments. The almost isotropic signal centered at g = 1.979 is instead associated to Ti^{3+} species.

Other minor features more evident in the conventionally sintered ceramic are attributable to the presence of a small amount of Mn^{2+} impurities, usually detectable even in pure $SrTiO_3$ systems and deriving from manganese substitution for titanium ions.[58]

As noted, the exposure to electric fields of La-doped $SrTiO_3$ has a remarkable effect on the defect structure of the material. In general, the doping with donor species, such as La^{3+} in the $SrTiO_3$ lattice, is compensated by the formation of vacancies of the alkali-earth cations.[41,43,59] The presence of these defects, which are known to improve the ionic diffusion in the crystal lattice[60−62]at high temperatures, likely induces the higher segregation of Sr^{2+} under the assistance of electric fields. As a matter of fact, $SrTiO_3$ treated with the same field conditions did not engender surface Sr enrichment to such extent.[29] Hence, the exposure to electric fields generates donor-doped perovskite lattices with a prominent A-site defective character. To counterbalance the presence of the negatively charged cationic vacancies (V''_{Sr}), ESR and XPS analyses indicated that singly ionized oxygen (O^-, i.e.,$O_o^\bullet$) is formed, both in the bulk and on the surface of the material more prominently than in the case of the conventionally treated system. As already suggested by West and co-workers,[21,22,63] when oxygen is underbonded in the vicinity of acceptor species (e.g., V''_{Sr}) under the exposure of an electric field, it can oxidize readily to O^-. The O^{2-} species is unstable in the gas phase and can only be stabilized in crystal lattices by the additional lattice energy of divalent Sr ions. Oxide ions within a strong A-site defective perovskite lattice are much less stabilized than in a defect-free environment and therefore subjected to oxidize promptly. In turn, the ionized electrons are trapped at surface states and determine the ionization of adsorbed oxygen molecules in O_2^{2-}/O^- species, as demonstrated by XPS analysis.

The defect structure changes in materials exposed to electric fields are shown to have significant effects on their electrical

DOI: 10.1021/acs.jpcc.9b04620
J. Phys. Chem. C 2019, 123, 16883−16892

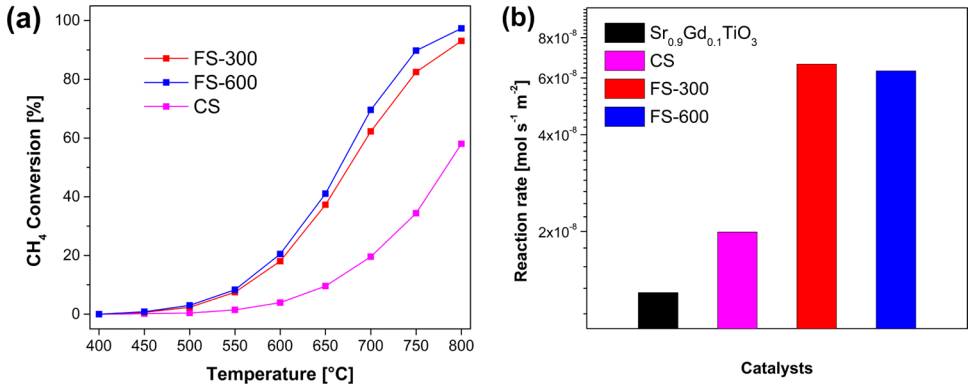

Figure 5. (a) Steady-state conversions obtained for the oxidation reaction of CH_4 over LSTO systems consolidated at different conditions. (b) CH_4 oxidation reaction rates of LSTO systems presented in this work compared with reported values by Oliva et al. for donor-doped $SrTiO_3$ ($Sr_{0.9}Gd_{0.1}TiO_3$) sintered in oxidizing conditions.[75] The values are retrieved at T = 550 °C and normalized by surface area.

properties.[63,64] To shed light on this subject, we investigated the consolidated La-doped $SrTiO_3$ by means of electrochemical impedance spectroscopy. All ceramics had density of 55%, and therefore their electrical behavior could be compared. The charge carrier density in donor-doped $SrTiO_3$ depends strongly on temperature, oxygen pressure, dopant concentration, and material pretreatment. The charge balance, expressed in the Kröger–Vink notation,[46] gives

$$2[V_O^{\bullet\bullet}] + [La_{Sr}^{\bullet}] - 2[V_{Sr}''] - n + p = 0 \quad (2)$$

where $V_O^{\bullet\bullet}$ represents the double positively charged oxygen vacancies, V_{Sr}'', the double negatively charged strontium vacancies, $La_{Sr}^{\bullet}$, the donor species, i.e., lanthanum ions, n, the electrons, and p, the holes.[43] Under oxidizing conditions, as those applied here, $[V_O^{\bullet\bullet}]$ and p are in general considered negligible and the ceramic behaves as an insulator.[43] This conductive behavior is governed by the donor and Sr vacancy concentration, determined by the synthesis and thermal treatment conditions.[43,59]

In accordance with the reports from the literature,[43,59] in the intermediate temperature range (up to 800 °C), we observed a constant total conductivity at variable pO_2 (Figure 4a). For the sake of completeness, it should be mentioned that the conductive measurements might be affected by the low grain size and densification degree (~55%) of the materials, which minimizes the grain contact.[65] That acknowledged, for the sample FS-600 can be inferred a slight positive slope, suggesting unexpected p-type conductivity. This effect is, however, reasonably supported by the ESR measurements, which evidenced a remarkable concentration of electron holes, i.e., O^- species, for this system and by several works in the literature on doped-titanate perovskite under the influence of electric field.[21,22,63,64]

Following the theory proposed by Meyer and Waser,[59] the lower conductivity of the field-exposed materials is ascribed to their higher concentration of Sr vacancies. Although these species are immobile at these temperatures[53] their density determines the effective donor dopant concentration and therefore the concentration of mobile electronic charge carriers (eq 2).

Moreover, the cationic vacancies might have an important effect for the lower activation energy for charge migration (Table 1, Figure 4b). LSTO consolidated under the influence of electric field exhibit constant values of migration enthalpy all over the investigated pO_2 range and lower of about 0.1 eV than for the conventionally treated counterpart. As largely reported in literature,[60,61,66−68] cationic vacancies in LSTO facilitates the charge carrier mobility through the perovskite lattice and therefore decreases the activation energy costs.

Another possibility, which cannot be excluded, is represented by the generation of mesoscopic size effects in LSTO nanocrystals. These phenomena, already introduced by Maier few years ago, suggest that when the grain size is of the same length scale as the space charge zone typical of grain boundaries, no unperturbed bulk exists anymore.[69,70] These effects have enormous impact on the electrical properties of $SrTiO_3$.[65,71,72] In particular, the downsizing of the grains to the nanoscale resulted in overlap of the Schottky barriers at grain boundaries and remarkable decrease of the space charge potential was observed. Although the space charge width cannot be determined in our case due to poor material densification, which prohibits the separation of bulk and grain boundary relaxations from the impedance spectra, such overlap may reasonably explain the lower migration energy encountered in field-exposed materials. Instead of being related to particle size effects, which in our case is constant for all the systems, the grain depletion might be originated by the much larger space charge region formed during the electric field-assisted treatment. With this respect, the absence of any grain boundary barriers was already found to induce remarkable enhancement of charge carrier mobility in La-doped $SrTiO_3$ with tailored defect distribution.[73,74]

The effect of the different point defect properties between conventionally and field-treated materials on their functional properties was investigated using the oxidation of methane, as a catalytic test reaction.

In Figure 5a, the light-off curves of the methane conversion are displayed. It can be immediately seen that the materials exposed to an electric field during consolidation show improved catalytic properties with respect to those of the conventionally treated counterpart.

FS samples reach almost complete conversion at 800 °C, whereas standard LSTO stops at 58%. Moreover, the temperature at which the half methane conversion (T_{50}) was obtained is more than 100 °C lower in field-consolidated materials (i.e., T_{50} values of CS, FS-300, and FS-600 samples are 782, 678, and 664 °C, respectively). The activation energy (E_a) values were estimated from Arrhenius-type plots (1000/T vs the reaction rate). The conventionally treated material has a larger E_a value that corresponds to the reaction rate than the flash-sintered one

DOI: 10.1021/acs.jpcc.9b04620
J. Phys. Chem. C 2019, 123, 16883−16892

(Table 1, Figure S8). This finding is in good agreement with the activation energy trend of charge carrier migration, as determined by impedance spectroscopy. Variation of the magnitude of the applied voltage did not engender a significant difference in observed activation energy, thus indicating that a similar reaction mechanism is involved in the methane oxidation over field-consolidated samples.

To confirm that this improved reactivity is not only due to increased specific surface area but also chemical effects, the reaction rate values normalized by specific surface area were compared for different samples. As shown in Figure 5b, the catalytic efficiency of field-consolidated materials is over 3 times higher than that of standard LSTO and other donor-doped perovskites. These observations are believed to be due to the unique defect properties of field-consolidated materials. Moreover, as their specific surface area is about twice as large as that of conventionally treated materials (Table 1), the overall reaction rate per gram of catalyst is almost 6 times faster.

In this regard, a central role is played by the large amount of O^- species present on the oxide surface (Figure 3b), which possess a highly oxidizing character[66] and are known to promote methane oxidation over oxides.[29,56,76] The enhanced catalysis kinetics is most likely motivated by the improved electronic mobility of the materials (Figure 4b), promoted by a combination of small grain size and high concentration of electron holes (e.g., $O_O^{\bullet}$, Figure 3d). A third contribution, possibly correlated with the first two, is the enhanced segregation of Sr at the material surface. As pointed out in our previous work,[29] as well as in several other literature reports,[77−80] when not consisting of thick dense layers, Sr-enriched surface phases are activated, which possess enhanced oxygen exchange kinetics, thus favoring the catalytic performance of the material. Moreover, it has been also recently shown that the high basicity of Sr-enriched $SrTiO_3$ surfaces plays a fundamental role in the dehydrogenation of methane and other organic compounds.[25,30,31] Similar to the NEMCA approach,[23] in field-assisted treatments as well, the modification of the catalytic properties occurs by manipulation of the state of charge of the oxygen species. However, if in NEMCA a change in the reactivity emerged only when a certain voltage was applied, the exposure to electric fields during consolidation permanently improves the catalytic performance of the materials, as verified by stability tests.[29] Through careful optimization of the field parameters, we believe that such a performance could be further improved and better catalytic conversion reached.

CONCLUSIONS

We showed how electric field-assisted treatments, usually employed as a sustainable and energy-saving ceramic processing technology, can be exploited to improve the functional properties of donor-doped $SrTiO_3$ with respect to conventional approaches. The accelerated consolidation of $La_{0.1}Sr_{0.9}TiO_3$ nanoparticles, induced by high electric fields (300−600 V cm^{-1}), promoted extensive segregation of Sr at the grain surface than in a conventionally treated system. In addition, field-treated systems exhibited high concentration of O^- defects both in bulk as well as on the material surface, as demonstrated by ESR and XPS results. Such hole centers are likely to be ascribed to the formation of underbonded oxygen within the perovskite lattice as a result of the Sr migration toward the surface. This enhanced defect concentration, in concomitance with the nanoscopic grain size of the field-consolidated materials, is probably one of the triggering factors of their improved charge carrier mobility, observed by impedance spectroscopy. The altered defect structure induced by the exposure to electric fields during consolidation clearly improved the catalytic performance of the materials. Using the total methane oxidation as a test reaction, we showed that the catalytic reaction rate was improved by a factor of 3 with respect to conventionally treated LSTO, concurrently with a significant decrease of the activation energy. We ascribed these findings to the higher concentration of highly oxidative O^- centers and the improved charge mobility, respectively. Hence, field-assisted treatments offer an interesting approach for modifying the defect structure of ceramic materials and their catalytic properties. Through careful tuning of the consolidation parameters (e.g., voltage, current, gas atmosphere) additional tailoring of structural and charge carrier properties might be reasonably possible, thus offering an attractive, forward-looking strategy for improving functional properties of ceramics in a sustainable fashion.

ASSOCIATED CONTENT

Supporting Information

The Supporting Information is available free of charge on the ACS Publications website at DOI: 10.1021/acs.jpcc.9b04620.

X-ray diffraction patterns of as-prepared $SrTiO_3$ and $La_{0.1}Sr_{0.9}TiO_3$ nanoparticles (Figure S1); plots for consolidation process (Figure S2), characterization of investigated LSTO samples by means of N_2 physisorption, SEM, TEM/EDX, XPS, and ESR spectroscopy (Figures S3−S7, Table S1); Arrhenius plots for catalytic methane oxidation over investigated samples (Figure S8) (PDF)

AUTHOR INFORMATION

Corresponding Author

*E-mail: simone.mascotto@chemie.uni-hamburg.de.

ORCID

Heshmat Noei: 0000-0003-1294-3527
WooChul Jung: 0000-0001-5266-3795
Simone Mascotto: 0000-0002-3503-6391

Notes

The authors declare no competing financial interest.

ACKNOWLEDGMENTS

B.K. and K.K. thank the MIN Graduate School International and the University of Hamburg for the financial support. S.L. and W.J. were financially supported by the Korea Institute of Energy Technology Evaluation and Planning (KETEP) and the Ministry of Trade, Industry & Energy (MOTIE) of the Republic of Korea (Nos. 20173010032120 and 20163030031850). We thank Andreas Kornowski of the University of Hamburg for electron microscopy measurements. Prof. Michael Fröba of the University of Hamburg is gratefully acknowledged for the support and fruitful discussions. M.D. thanks Prof. Roberto Scotti of the University of Milano-Bicocca for a valuable discussion on the ESR section.

REFERENCES

(1) Dahl, J. A.; Maddux, B. L. S.; Hutchison, J. E. Toward Greener Nanosynthesis. *Chem. Rev.* **2007**, *107*, 2228−2269.

(2) Moreira, M. L.; Mambrini, G. P.; Volanti, D. P.; Leite, E. R.; Orlandi, M. O.; Pizani, P. S.; Mastelaro, V. R.; Paiva-Santos, C. O.; Longo, E.; Varela, J. A. Hydrothermal Microwave: A New Route to

DOI: 10.1021/acs.jpcc.9b04620
J. Phys. Chem. C 2019, 123, 16883−16892

Obtain Photoluminescent Crystalline $BaTiO_3$ Nanoparticles. *Chem. Mater.* **2008**, *20*, 5381−5387.
(3) Bilecka, I.; Niederberger, M. Microwave Chemistry for Inorganic Nanomaterials Synthesis. *Nanoscale* **2010**, *2*, 1358.
(4) Mascotto, S.; Tsetsgee, O.; Muller, K.; Maccato, C.; Smarsly, B.; Brandhuber, D.; Tondello, E.; Gross, S. Effect of Microwave Assisted and Conventional Thermal Heating on the Evolution of Nanostructured Inorganic-Organic Hybrid Materials to Binary ZrO_2-SiO_2 Oxides. *J. Mater. Chem.* **2007**, *17*, 4387−4399.
(5) Guillon, O.; Elsässer, C.; Gutfleisch, O.; Janek, J.; Korte-Kerzel, S.; Raabe, D.; Volkert, C. A. Manipulation of Matter by Electric and Magnetic Fields: Toward Novel Synthesis and Processing Routes of Inorganic Materials. *Mater. Today* **2018**, *21*, 527−536.
(6) Molodov, D. A.; Bozzolo, N. Observations on the Effect of a Magnetic Field on the Annealing Texture and Microstructure Evolution in Zirconium. *Acta Mater.* **2010**, *58*, 3568−3581.
(7) Rheinheimer, W.; Parras, J. P.; Preusker, J.-H.; De Souza, R. A.; Hoffmann, M. J. Grain Growth in Strontium Titanate in Electric Fields: The Impact of Space-Charge on the Grain-Boundary Mobility. *J. Am. Ceram. Soc.* **2019**, *102*, 3779−3790.
(8) Biesuz, M.; Sglavo, V. M. Current-Induced Abnormal and Oriented Grain Growth in Corundum upon Flash Sintering. *Scr. Mater.* **2018**, *150*, 82−86.
(9) Cho, J.; Li, Q.; Wang, H.; Fan, Z.; Li, J.; Xue, S.; Vikrant, K. S. N.; Wang, H.; Holland, T. B.; Mukherjee, A. K.; et al. High Temperature Deformability of Ductile Flash-Sintered Ceramics via in-Situ Compression. *Nat. Commun.* **2018**, *9*, No. 2063.
(10) Vendrell, X.; West, A. R. Induced P-Type Semiconductivity in Yttria-stabilized Zirconia. *J. Am. Ceram. Soc.* **2019**, DOI: 10.1111/jace.16492.
(11) Rheinheimer, W.; Phuah, X. L.; Wang, H.; Lemke, F.; Hoffmann, M. J.; Wang, H. The Role of Point Defects and Defect Gradients in Flash Sintering of Perovskite Oxides. *Acta Mater.* **2019**, *165*, 398−408.
(12) Biesuz, M.; Sglavo, V. M. Flash Sintering of Ceramics. *J. Eur. Ceram. Soc.* **2019**, *39*, 115−143.
(13) Becker, M. Z.; Shomrat, N.; Tsur, Y. Recent Advances in Mechanism Research and Methods for Electric-Field-Assisted Sintering of Ceramics. *Adv. Mater.* **2018**, *30*, No. 1706369.
(14) Yu, M.; Grasso, S.; Mckinnon, R.; Saunders, T.; Reece, M. J. Review of Flash Sintering: Materials, Mechanisms and Modelling. *Adv. Appl. Ceram.* **2017**, *116*, 24−60.
(15) Cologna, M.; Francis, J. S. C.; Raj, R. Field Assisted and Flash Sintering of Alumina and Its Relationship to Conductivity and MgO-Doping. *J. Eur. Ceram. Soc.* **2011**, *31*, 2827−2837.
(16) Zhang, Y.; Nie, J.; Chan, J. M.; Luo, J. Probing the Densification Mechanisms during Flash Sintering of ZnO. *Acta Mater.* **2017**, *125*, 465−475.
(17) Ji, W.; Parker, B.; Falco, S.; Zhang, J. Y.; Fu, Z. Y.; Todd, R. I. Ultra-Fast Firing: Effect of Heating Rate on Sintering of 3YSZ, with and without an Electric Field. *J. Eur. Ceram. Soc.* **2017**, *37*, 2547−2551.
(18) Karakuscu, A.; Cologna, M.; Yarotski, D.; Won, J.; Francis, J. S. C.; Raj, R.; Uberuaga, B. P. Defect Structure of Flash-Sintered Strontium Titanate. *J. Am. Ceram. Soc.* **2012**, *95*, 2531−2536.
(19) Gaur, A.; Sglavo, V. M. Densification of La0.6Sr0.4Co0.2-Fe0.8O3 Ceramic by Flash Sintering at Temperature Less than 100 °C. *J. Mater. Sci.* **2014**, *49*, 6321−6332.
(20) Shomrat, N.; Baltianski, S.; Dor, E.; Tsur, Y. The Influence of Doping on Flash Sintering Conditions in SrTi1-XFexO3. *J. Eur. Ceram. Soc.* **2017**, *37*, 179−188.
(21) Gil Escrig, L.; Prades, M.; Beltrán, H.; Cordoncillo, E.; Masõ, N.; West, A. R. Voltage-Dependent Bulk Resistivity of SrTiO3: Mg Ceramics. *J. Am. Ceram. Soc.* **2014**, *97*, 2815−2824.
(22) Masó, N.; Prades, M.; Beltrán, H.; Cordoncillo, E.; Sinclair, D. C.; West, A. R. Field Enhanced Bulk Conductivity of Acceptor-Doped $BaTi_{1-x}Ca_xO_{3-x}$ Ceramics. *Appl. Phys. Lett.* **2010**, *97*, No. 062907.
(23) Vayenas, C. G.; Bebelis, S.; Yentekakis, I. V.; Lintz, H.-G. Non-Faradaic Electrochemical Modification of Catalytic Activity: A Status Report. *Catal. Today* **1992**, *11*, 303−438.
(24) Vayenas, C. G.; Bebelis, S.; Neophytides, S. Non-Faradaic Electrochemical Modification of Catalytic Activity. *J. Phys. Chem. A* **1988**, *92*, 5083−5085.
(25) Polo-Garzon, F.; Yang, S. Z.; Fung, V.; Foo, G. S.; Bickel, E. E.; Chisholm, M. F.; Jiang, D. E.; Wu, Z. Controlling Reaction Selectivity through the Surface Termination of Perovskite Catalysts. *Angew. Chem., Int. Ed.* **2017**, *56*, 9820−9824.
(26) Foo, G. S.; Hood, Z. D.; Wu, Z. Shape Effect Undermined by Surface Reconstruction: Ethanol Dehydrogenation over Shape-Controlled $SrTiO_3$ Nanocrystals. *ACS Catal.* **2018**, *8*, 555−565.
(27) Kayaalp, B. E.; Lee, Y. J.; Kornowski, A.; Gross, S.; D'Arienzo, M.; Mascotto, S. Cooperative Assembly Synthesis of Mesoporous SrTiO 3 with Enhanced Photocatalytic Properties. *RSC Adv.* **2016**, *6*, 90401−90409.
(28) Kayaalp, B.; Lee, S.; Klauke, K.; Jongsu, S.; Nodari, L.; Kornowski, A.; Jung, W.; Mascotto, S. Template-Free Mesoporous La0.3Sr0.7FexTi1-XO3±δ for CH4 and CO Oxidation Catalysis. *Appl. Catal., B* **2019**, *245*, 536−545.
(29) Klauke, K.; Kayaalp, B.; Biesuz, M.; Iannaci, A.; Sglavo, V. M.; D'Arienzo, M.; Lee, S.; Jongsu, S.; Jung, W.; Mascotto, S. Enhancement of the SrTiO3 Surface Reactivity by Exposure to Electric Fields. *ChemNanoMat* **2019**, DOI: 10.1002/cnma.201900201.
(30) Bai, L.; Polo-Garzon, F.; Bao, Z.; Luo, S.; Moskowitz, B. M.; Tian, H.; Wu, Z. Impact of Surface Composition of $SrTiO_3$ Catalysts for Oxidative Coupling of Methane. *ChemCatChem* **2019**, *11*, 2107−2117.
(31) Polo-Garzon, F.; Fung, V.; Liu, X.; Hood, Z. D.; Bickel, E. E.; Bai, L.; Tian, H.; Foo, G. S.; Chi, M.; Jiang, D.; et al. Understanding the Impact of Surface Reconstruction of Perovskite Catalysts on CH_4 Activation and Combustion. *ACS Catal.* **2018**, *8*, 10306−10315.
(32) Verbraeken, M. C.; Ramos, T.; Agersted, K.; Ma, Q.; Savaniu, C. D.; Sudireddy, B. R.; Irvine, J. T. S.; Holtappels, P.; Tietz, F. Modified Strontium Titanates: From Defect Chemistry to SOFC Anodes. *RSC Adv.* **2015**, *5*, 1168−1180.
(33) Park, K.; Son, J. S.; Woo, S. I.; Shin, K.; Oh, M.-W.; Park, S.-D.; Hyeon, T. Colloidal Synthesis and Thermoelectric Properties of La-Doped SrTiO3 Nanoparticles. *J. Mater. Chem. A* **2014**, *2*, 4217.
(34) Dolcet, P.; Diodati, S.; Zorzi, F.; Voepel, P.; Seitz, C.; Smarsly, B. M.; Mascotto, S.; Nestola, F.; Gross, S. Very Fast Crystallisation of MFe2O4 Spinel Ferrites (M = Co, Mn, Ni, Zn) under Low Temperature Hydrothermal Conditions: A Time-Resolved Structural Investigation. *Green Chem.* **2018**, *20*, 2257−2268.
(35) Diodati, S.; Nodari, L.; Natile, M. M.; Caneschi, A.; de Julián Fernández, C.; Hoffmann, C.; Kaskel, S.; Lieb, A.; Di Noto, V.; Mascotto, S.; et al. Coprecipitation of Oxalates: An Easy and Reproducible Wet-Chemistry Synthesis Route for Transition-Metal Ferrites. *Eur. J. Inorg. Chem.* **2014**, *2014*, 875−887.
(36) Chen, Y.; Jung, W.; Cai, Z.; Kim, J. J.; Tuller, H. L.; Yildiz, B. Impact of Sr Segregation on the Electronic Structure and Oxygen Reduction Activity of SrTi1-XFexO3 Surfaces. *Energy Environ. Sci.* **2012**, *5*, 7979−7988.
(37) Ouyang, S.; Li, P.; Xu, H.; Tong, H.; Liu, L.; Ye, J. Bifunctional-Nanotemplate Assisted Synthesis of Nanoporous SrTiO 3 Photocatalysts Toward Efficient Degradation of Organic Pollutant. *ACS Appl. Mater. Interfaces* **2014**, *6*, 22726−22732.
(38) Brunauer, S.; Emmett, P. H.; Teller, E. Adsorption of Gases in Multimolecular Layers. *J. Am. Chem. Soc.* **1938**, *60*, 309−319.
(39) Stierle, A.; Keller, T. F.; Noei, H.; Vonk, V.; Roehlsberger, R. DESY NanoLab. *J. Large-Scale Res. Facil.* **2016**, *2*, A76.
(40) Adamski, A.; Spałek, T.; Sojka, Z. Application of EPR Spectroscopy for Elucidation of Vanadium Speciation in VOx/ZrO2 Catalysts Subject to Redox Treatment. *Res. Chem. Intermed.* **2003**, *29*, 793−804.
(41) Meyer, R.; Waser, R.; Helmbold, J.; Borchardt, G. Cationic Surface Segregation in Donor-Doped SrTiO3under Oxidizing Conditions. *J. Electroceram.* **2002**, *9*, 101−110.
(42) Yaremchenko, A. A.; Naumovich, E. N.; Patrício, S. G.; Merkulov, O. V.; Patrakeev, M. V.; Frade, J. R. Rare-Earth-Substituted Strontium Titanate: Insight into Local Oxygen-Rich Structures and Redox Kinetics. *Inorg. Chem.* **2016**, *55*, 4836−4849.

DOI: 10.1021/acs.jpcc.9b04620
J. Phys. Chem. C 2019, 123, 16883−16892

(43) Meyer, R.; Zurhelle, A. F.; De Souza, R. A.; Waser, R.; Gunkel, F. Dynamics of the Metal-Insulator Transition of Donor-Doped SrTiO3. *Phys. Rev. B* **2016**, *94*, No. 115408.
(44) Koo, B.; Kwon, H.; Kim, Y.; Seo, H. G.; Han, J. W.; Jung, W. Enhanced Oxygen Exchange of Perovskite Oxide Surfaces through Strain-Driven Chemical Stabilization. *Energy Environ. Sci.* **2018**, *11*, 71−77.
(45) Koo, B.; Kim, K.; Kim, J. K.; Kwon, H.; Han, J. W.; Jung, W. Sr Segregation in Perovskite Oxides: Why It Happens and How It Exists. *Joule* **2018**, *2*, 1476−1499.
(46) Kröger, F. A.; Vink, H. J. Relations between the Concentrations of Imperfections in Crystalline Solids. *Solid State Phys.* **1956**, *3*, 307−435.
(47) Meyer, R.; Waser, R.; Helmbold, J.; Borchardt, G. Observation of Vacancy Defect Migration in the Cation Sublattice of Complex Oxides by 18O Tracer Experiments. *Phys. Rev. Lett.* **2003**, *90*, No. 105901.
(48) Crawford, J.; Jacobs, P. Point Defect Energies for Strontium Titanate: A Pair-Potentials Study. *J. Solid State Chem.* **1999**, *144*, 423−429.
(49) De Souza, R. A. Oxygen Diffusion in SrTiO3 and Related Perovskite Oxides. *Adv. Funct. Mater.* **2015**, *25*, 6326−6342.
(50) Chaim, R.; Chevallier, G.; Weibel, A.; Estournès, C. Flash Sintering of Dielectric Nanoparticles as a Percolation Phenomenon through a Softened Film. *J. Appl. Phys.* **2017**, *121*, No. 145103.
(51) Naik, K. S.; Sglavo, V. M.; Raj, R. Flash Sintering as a Nucleation Phenomenon and a Model Thereof. *J. Eur. Ceram. Soc.* **2014**, *34*, 4063−4067.
(52) Narayan, J. A New Mechanism for Field-Assisted Processing and Flash Sintering of Materials. *Scr. Mater.* **2013**, *69*, 107−111.
(53) Moos, R.; Hardtl, K. H. Defect Chemistry of Donor-Doped and Undoped Strontium Titanate Ceramics between 1000 Degrees and 1400 Degrees C. *J. Am. Ceram. Soc.* **1997**, *80*, 2549−2562.
(54) Gömann, K.; Borchardt, G.; Schulz, M.; Gömann, A.; Maus-Friedrichs, W.; Lesage, B.; Kaïtasov, O.; Hoffmann-Eifert, S.; Schneller, T. Sr Diffusion in Undoped and La-Doped $SrTiO_3$ Single Crystals under Oxidizing Conditions. *Phys. Chem. Chem. Phys.* **2005**, *7*, 2053−2060.
(55) Che, M.; Tench, A. J. Characterization and Reactivity of Mononuclear Oxygen Species on Oxide Surfaces. *Adv. Catal.* **1982**, *31*, 77−133.
(56) Oliva, C.; Bonoldi, L.; Cappelli, S.; Fabbrini, L.; Rossetti, I.; Forni, L. Effect of Preparation Parameters on SrTiO $3\pm\delta$ Catalyst for the Flameless Combustion of Methane. *J. Mol. Catal. A: Chem.* **2005**, *226*, 33−40.
(57) Rubio, J. O.; Tohver, H. T.; Chen, Y.; Abraham, M. M. Trapped-Hole Defects in SrO. *Phys. Rev. B* **1976**, *14*, 5466−5472.
(58) Harrigan, W. L.; Michaud, S. E.; Lehuta, K. A.; Kittilstved, K. R. Tunable Electronic Structure and Surface Defects in Chromium-Doped Colloidal $SrTiO_{3-\delta}$ Nanocrystals. *Chem. Mater.* **2016**, *28*, 430−433.
(59) Meyer, R.; Waser, R. Resistive Donor-Doped SrTiO3 Sensors: I, Basic Model for a Fast Sensor Response. *Sens. Actuators, B* **2004**, *101*, 335−345.
(60) Tsekouras, G.; Irvine, J. T. S. The Role of Defect Chemistry in Strontium Titanates Utilised for High Temperature Steam Electrolysis. *J. Mater. Chem.* **2011**, *21*, 9367.
(61) Konysheva, E. Y.; Xu, X.; Irvine, J. T. S. On the Existence of A-Site Deficiency in Perovskites and Its Relation to the Electrochemical Performance. *Adv. Mater.* **2012**, *24*, 528−532.
(62) Neagu, D.; Tsekouras, G.; Miller, D. N.; Ménard, H.; Irvine, J. T. S. In Situ Growth of Nanoparticles through Control of Non-Stoichiometry. *Nat. Chem.* **2013**, *5*, 916−923.
(63) Masó, N.; West, A. R. Electronic Conductivity in Yttria-Stabilized Zirconia under a Small Dc Bias. *Chem. Mater.* **2015**, *27*, 1552−1558.
(64) Masó, N.; Beltrán, H.; West, A. R.; Prades, M.; Cordoncillo, E. Voltage-Dependent Low-Field Bulk Resistivity in BaTiO3:Zn Ceramics. *J. Am. Ceram. Soc.* **2010**, *93*, 500−505.
(65) Gregori, G.; Heinze, S.; Lupetin, P.; Habermeier, H. U.; Maier, J. Seebeck Coefficient and Electrical Conductivity of Mesoscopic Nanocrystalline SrTiO3. *J. Mater. Sci.* **2013**, *48*, 2790−2796.
(66) Zhu, Y.; Zhou, W.; Yu, J.; Chen, Y.; Liu, M.; Shao, Z. Enhancing Electrocatalytic Activity of Perovskite Oxides by Tuning Cation Deficiency for Oxygen Reduction and Evolution Reactions. *Chem. Mater.* **2016**, *28*, 1691−1697.
(67) Battle, P. D.; Bennett, J. E.; Sloan, J.; Tilley, R. J. D.; Vente, J. F. A-Site Cation-Vacancy Ordering in Sr(1-3x/2)La(x)TiO3: A Study by HRTEM. *J. Solid State Chem.* **2000**, *149*, 360−369.
(68) Striker, T.; Ruud, J. A.; Gao, Y.; Heward, W. J.; Steinbruchel, C. A-Site Deficiency, Phase Purity and Crystal Structure in Lanthanum Strontium Ferrite Powders. *Solid State Ionics* **2007**, *178*, 1326−1336.
(69) Maier, J. Nanoionics: Ion Transport and Electrochemical Storage in Confined Systems. *Nat. Mater.* **2005**, *4*, 805−815.
(70) Maier, J. Pushing Nanoionics to the Limits: Charge Carrier Chemistry in Extremely Small Systems. *Chem. Mater.* **2014**, *26*, 348−360.
(71) Lupetin, P.; Gregori, G.; Maier, J. Mesoscopic Charge Carriers Chemistry in Nanocrystalline SrTiO3. *Angew. Chem., Int. Ed.* **2010**, *49*, 10123−10126.
(72) Balaya, P.; Jamnik, J.; Fleig, J.; Maier, J. Mesoscopic Electrical Conduction in Nanocrystalline SrTiO3. *Appl. Phys. Lett.* **2006**, *88*, No. 062109.
(73) Son, J.; Moetakef, P.; Jalan, B.; Bierwagen, O.; Wright, N. J.; Engel-Herbert, R.; Stemmer, S. Epitaxial SrTiO3films with Electron Mobilities Exceeding 30,000 Cm2V-1s-1. *Nat. Mater.* **2010**, *9*, 482−484.
(74) Kozuka, Y.; Hikita, Y.; Bell, C.; Hwang, H. Y. Dramatic Mobility Enhancements in Doped SrTiO3thin Films by Defect Management. *Appl. Phys. Lett.* **2010**, *97*, No. 012107.
(75) Oliva, C.; Cappelli, S.; Rossetti, I.; Kryukov, A.; Bonoldi, L.; Forni, L. Effect of M Ion Oxidation State in $Sr_{1-x}M_xTiO_3$ Perovskites in Methane Catalytic Flameless Combustion. *J. Mol. Catal. A: Chem.* **2006**, *245*, 55−61.
(76) Aika, K.; Lunsford, J. H. Surface Reactions of Oxygen Ions. I. Dehydrogenation of Alkanes by Oxygen(1-) Ions on Magnesium Oxide. *J. Phys. Chem. A* **1977**, *81*, 1393−1398.
(77) Li, Y.; Zhang, W.; Zheng, Y.; Chen, J.; Yu, B.; Chen, Y.; Liu, M. Controlling Cation Segregation in Perovskite-Based Electrodes for High Electro-Catalytic Activity and Durability. *Chem. Soc. Rev.* **2017**, *46*, 6345−6378.
(78) Mutoro, E.; Crumlin, E. J.; Biegalski, M. D.; Christen, H. M.; Shao-Horn, Y. Environmental Science Enhanced Oxygen Reduction Activity on Surface-Decorated Perovskite Thin Films for Solid Oxide Fuel Cells. *Energy Environ. Sci.* **2011**, *4*, 3689−3696.
(79) la O', G. J.; Savinell, R. F.; Shao-Horn, Y. Activity Enhancement of Dense Strontium-Doped Lanthanum Manganite Thin Films under Cathodic Polarization: A Combined AES and XPS Study. *J. Electrochem. Soc.* **2009**, *156*, B771.
(80) Baumann, F. S.; Fleig, J.; Konuma, M.; Starke, U.; Habermeier, H.-U.; Maier, J. Strong Performance Improvement of La0.6Sr0.4Co0.8-Fe0.2O3−δ SOFC Cathodes by Electrochemical Activation. *J. Electrochem. Soc.* **2005**, *152*, A2074−A2079.

DOI: 10.1021/acs.jpcc.9b04620
J. Phys. Chem. C 2019, 123, 16883−16892